Supplementary Information

Top-down Architecture of Magnetized Micro-cilia and Conductive Micro-domes as Full Bionic Electronic Skin for De-coupled Multidimensional Tactile Perception

Fengming Hu, Qian Zhou, Ruolin Liu, Yanfei Zhu, Yuanzhe Liang, Dan Fang, Bing Ji, Zhiming Chen,* Jianyi Luo,* and Bingpu Zhou*

Fengming Hu, Ruolin Liu, Yuanzhe Liang, Dan Fang, Prof. Bingpu Zhou
Joint Key Laboratory of the Ministry of Education, Institute of Applied Physics and Materials Engineering, University of Macau, Avenida da Universidade, Taipa, Macau 999078, China
E-mail: bpzhou@um.edu.mo

Fengming Hu, Yanfei Zhu, Dr. Zhiming Chen, Prof. Jianyi Luo
Research Center of Flexible Sensing Materials and Devices, School of Applied Physics and Materials, Wuyi University, Jiangmen 529020, China
E-mail: chenzhiming@wyu.edu.cn; luojiany@mail3.sysu.edu.cn

Dr. Qian Zhou
School of Physics and Electronics, Central South University, Changsha 410083, China

Prof. Bing Ji
School of Physics and Electronics, Hunan Normal University, Changsha 410081, China

Contents

Supplementary Video Captions.

Video S1. The voltage signal response of the dual-mode sensor when exposed to mechanical presses with/without duration. In the video, a micro-displacement platform is used to simulate repeated actions of sustained and non-sustained duration presses, demonstrating that the dual-mode sensor can mimic the response mechanism of human's RA/SA receptors. The video was processed with 4X speed for play.

Video S2. Response of the dual-mode sensor to the tangential force applied by finger sliding is recorded. Thanks to the high aspect ratio and excellent deformability of the MMCA structure, the FBE-skin also can respond to shear mechanical stimuli in the plane. The video was processed with 1.5X speed for play.

Video S3. Records of MMCA deformation of FBE-skin under lateral and normal airflow. The video shows that the FBE-skin based on the MMCA can effectively respond to non-contact airflow in addition to contact stress.

Video S4. Demonstration of the FBE-skin array for recognition of sliding speeds ($V_0<V_1<V_2$) and Routes 1, 2. In the video, the finger slides at a speed V_0 across the fourth row of the array device from left to right (route 1) and vertically from top to bottom across the first column of the device (route 2). During this process, the voltage signals of the device were collected by a multiplexed data acquisition equipment and real-time presented on the LabVIEW interface, displaying these sliding trajectories. The color of the blocks in the intensity map and the height variation of the histograms in the 3D surface are consistent. Simultaneously, when the finger slides along route 2 at speeds V_1 and V_2, the device generates different voltage signals based on the color of the blocks and the height of the histograms displayed on the interface. In summary, this video proves that the FBE-skin array can mimic the human skin's ability to respond to sliding speeds and its application in recording motion trajectories.

Video S5. Demonstration of the FBE-skin array device for perception of spatial distribution of the airflow. The video records scenarios involving airflow from different directions and intensities: lateral airflow sources located in the upper right corner at distances D_1 and D_2 from the corresponding sensor units, and a vertically downward airflow source situated directly above. The color distribution of the block in the intensity diagram and the height distribution of the histogram on the three-dimensional surface represent the spatial distribution of the airflow. The orientation of the airflow can be determined by observing the positions where the colors in the grid exhibit concentrated changes.

Video S6. Demonstration of the FBE-skin array device's proximity perception and simulation of the human-skin by issuing a warning signal to indicate harmful touch. Applying a minimal pressure to the array device to mimic the response of before physical contact human-skin, only the MMCA sensing components exhibit a response (non-zero voltage change, and approximately zero current change). The corresponding alert light on the LabVIEW interface remains off. Gradually increasing the pressure load to a moderate level simulates the finger touching the epidermis-dermis layer of the skin with different pressures. At this moment, both the MMCA and MDA sensing components generate voltage and current signals. The alert light on the LabVIEW interface turns green, also indicating no harm but providing a warning for potential impact. Further increasing the pressure load to a level that could potentially damage the skin, the current signal from the micro-dome component increases to the threshold, triggering the alert light on the LabVIEW interface to turn red. This situation triggering the red alert light is repeated for three times.

Supplementary Figures.

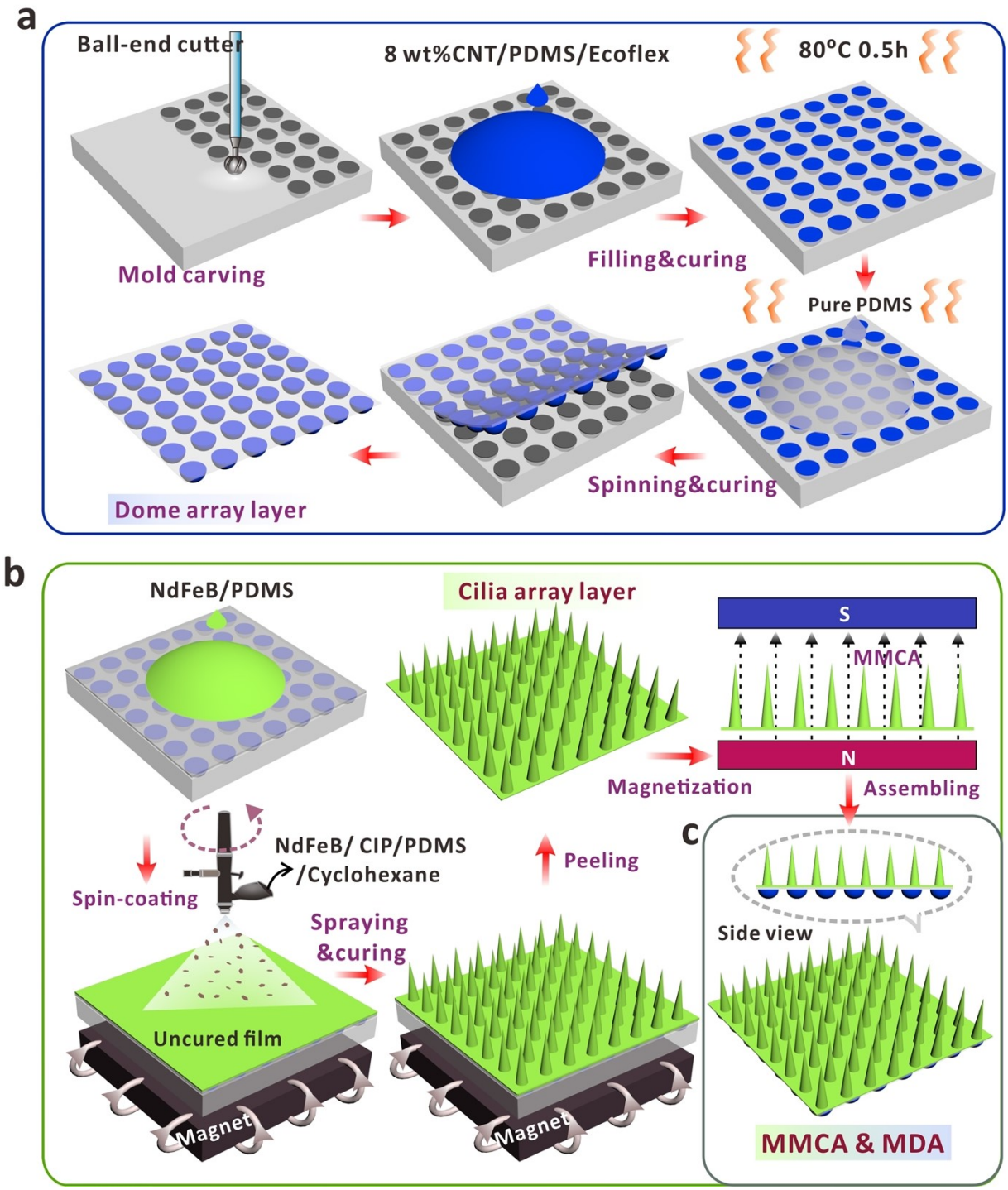

Figure S1. Schematic diagram of the fabrication process for the full bionic E-skin (FBE-skin). (a) Preparation of conductive CNT/PDMS/Ecoflex micro-dome array (MDA) layer. (b) Preparation of NdFeB/CIP/PDMS magnetized micro-cilia array (MMCA) layer. (c) Top-down assembly of the MMCA and MDA layers as FBE-skin.

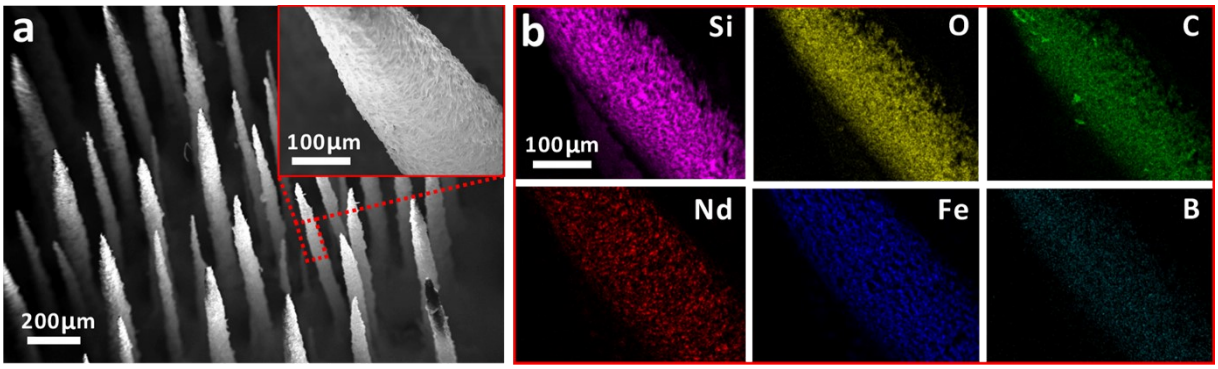

Figure S2. (a) SEM image and (b) EDX mapping results of the MMCA layer. The elements of Si, O, C, Nd, Fe and B indicate the uniform distribution of different components within the micro-cilia matrix.

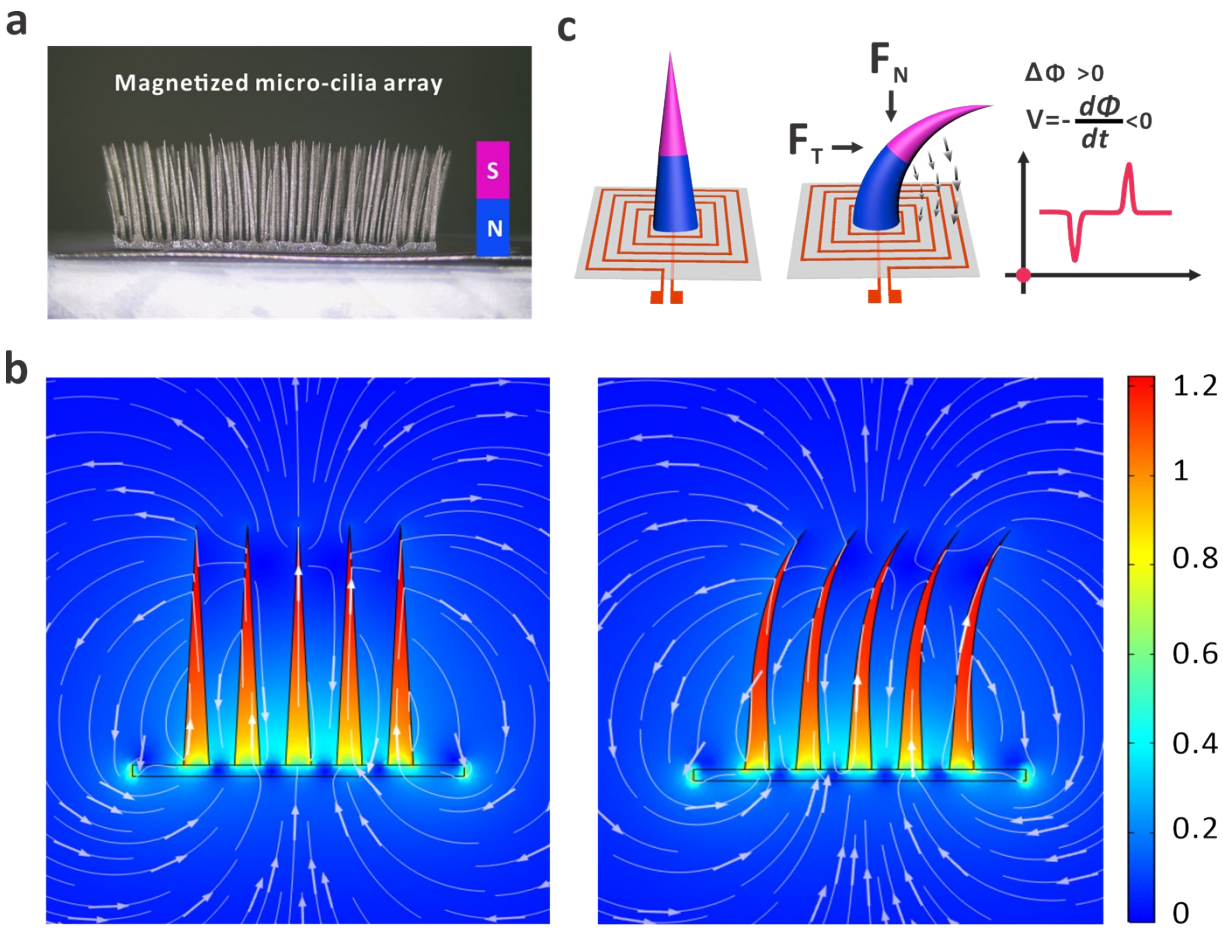

Figure S3. (a) Optical image of the vertically aligned magnetized micro-cilia array. (b) Simulation of the variation in magnetic field intensity during the bending process of the micro-cilia array. (c) Schematic diagram of magnetic flux changes and corresponding voltage generation when the micro-cilia are subjected to normal (F_N) and tangential (F_T) forces.

With the incorporated NdFeB components, the magnetized micro-cilia can serve as the flexible permanent magnets in the wearable system. When exposed to external mechanical stimuli, the deformation of the MMCA would thus lead to the variation of spatial magnetic flux, which can be perceived by the coil electrode underneath. As the schematic diagram shows, the voltage can be instantaneously induced based on the law of electromagnetic induction. Unlike conventional pressure sensors which are mainly focusing on the detection in normal direction, the three-dimensional (3D) MMCA can perceive both the normal and tangential forces thanks to the high aspect ratios. This capability allows the FBE-skin to fully mimic the functionality of human skin and achieve a more vivid sensing experience.

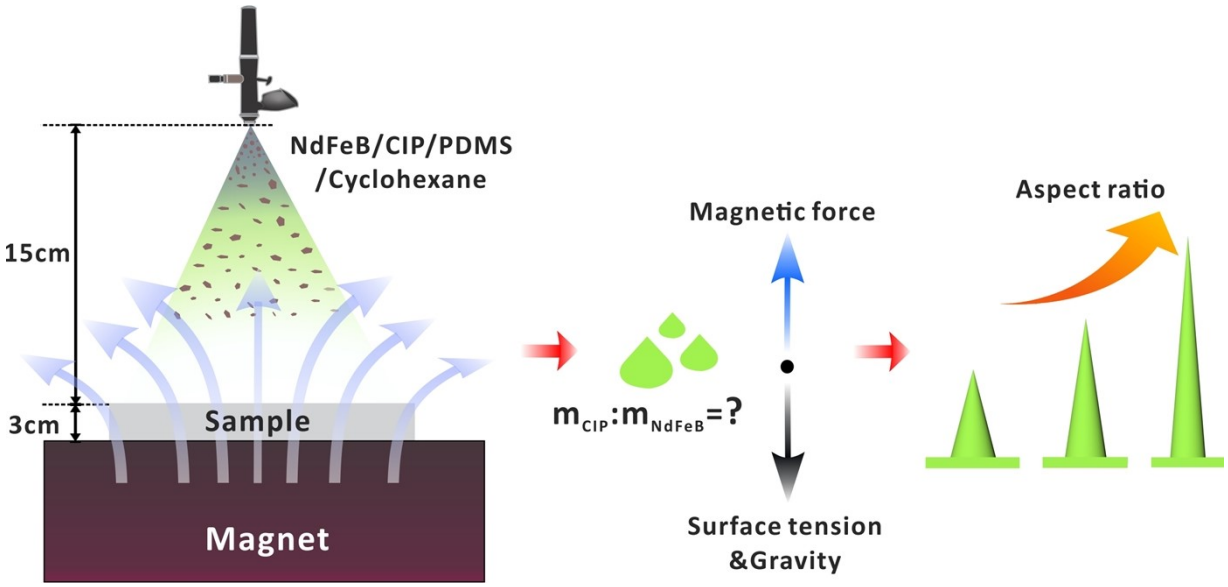

Figure S4. Schematic diagram of the preparation setup for the micro-cilia and the parameters that can be applied to adjust the morphological property (e.g. aspect ratio) of the MMCA.

In the preparation of the micro-cilia array, the distance from the spraying nozzle to the sample stage was fixed at 15 cm, and the distance between the sample and the surface of the permanent magnet was 3 cm. During the micro-cilia formation, the droplets accumulated along the direction of the magnetic field lines. Owing to the combinational effects from the intrinsic gravity, surface tension, and the upward magnetic force by the magnet, the micro-cilia with a cone-shaped structure can be obtained spontaneously. The mass ratio of different components within the solution can thus provide an effective method to regulate the morphological properties of the micro-cilia, *e.g.* the aspect ratio. Furthermore, via regulating the percentage of NdFeB particles, the remanence after magnetization can be controlled, which finally affects the intensity of the induced voltage because of the magnetic flux change.

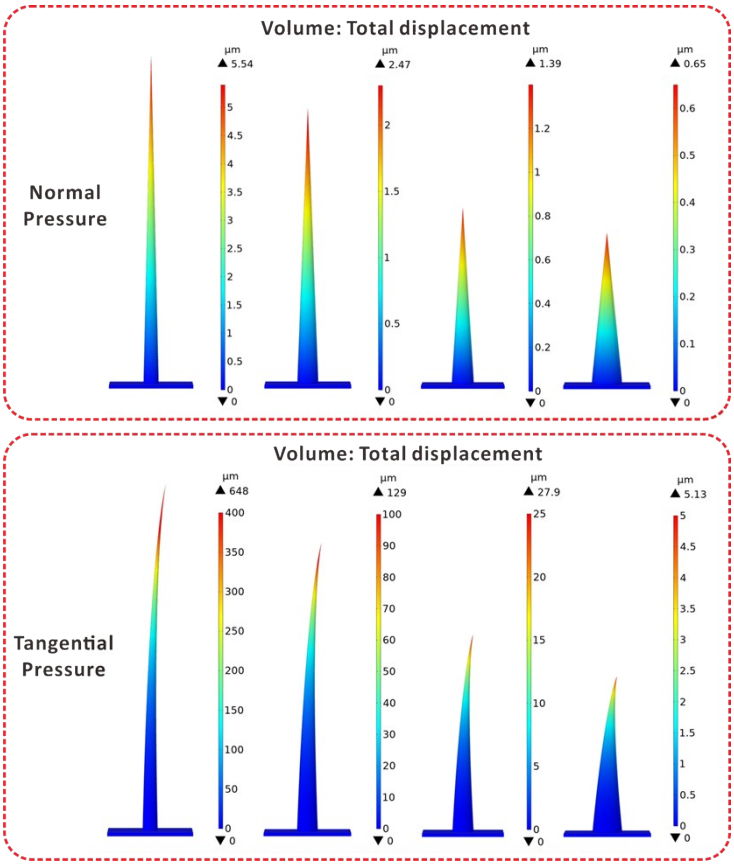

Figure S5. Simulation results of the micro-cilia displacement under the same normal and tangential pressures.

The cone-shaped models were built in COMSOL Multiphysics software using four typical sizes of micro-cilia prototypes (aspect ratios of 21.8, 15.0, 9.1, and 5.8). In the simulation, PDMS with the same properties (E=750 kPa, υ=0.49) was selected as the material for the micro-structures. Here, E is the elastic modulus and υ is the Poisson's ratio. The physical interfaces of the refined dimensions were controlled using a fine tetrahedral mesh. The Solid Mechanics module of structural mechanics was employed to simulate the same tangential and normal pressures. To simulate the displacement in both directions, the applied force was set at 1 μN. Subsequently, the displacements of the micro-cilia were computed to demonstrate the relationship between the deformation magnitude and the aspect ratio of the micro-cilia. Regardless of normal or tangential pressures, micro-cilia with a higher aspect ratio are more prone to morphological deformation, indicating that the micro-cilia in larger aspect ratios are more sensitive to subtle pressures with lower detection limits.

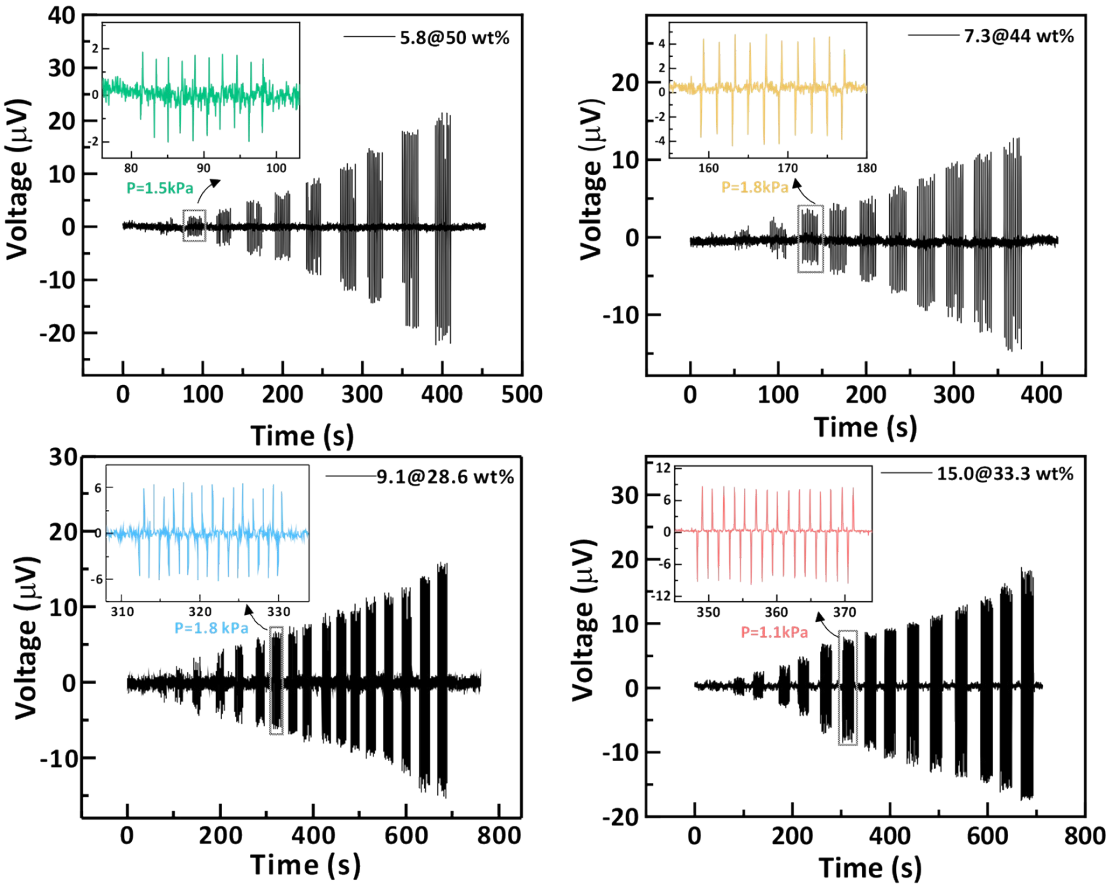

Figure S6. Real-time response of the E-skin when the MMCA devices were applied with different dynamic pressure up to 30 kPa. The inset provides an enlarged voltage profile over time in one cycle. The compression speed is set at 30 mm/s.

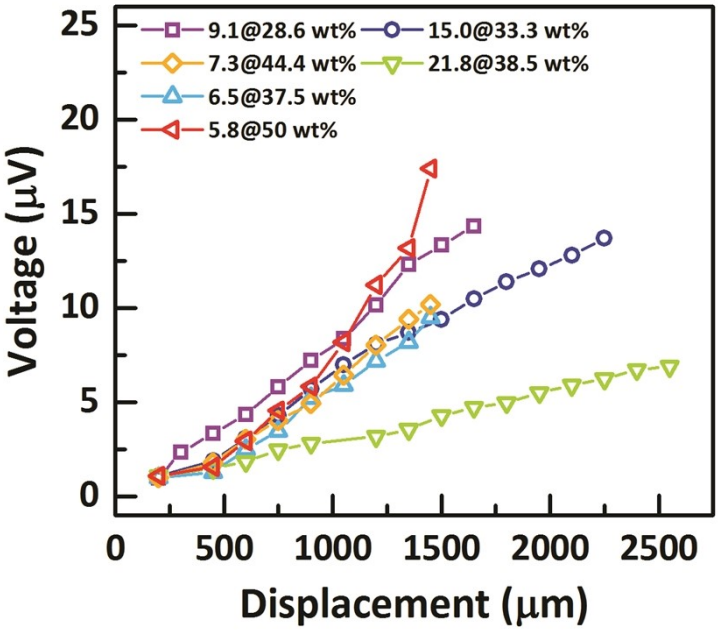

Figure S7. The relationship between the deformation and the output voltage of MMCA devices with different aspect ratios under different pressures.

The plots provide a direct information about the relationship between the micro-cilia deformation and the induced voltage. For the micro-cilia with a smaller aspect ratio (*e.g.* 5.8), the related larger amount of magnetic flux within a unit volume can provide a higher voltage. Under the same displacement, however, the voltage signals from the micro-cilia with a larger aspect ratio are relatively smaller. This is because of the thinner morphology of such micro-cilia, and the magnetic flux within a unit volume is thus limited. The results indicate that the optimization of micro-cilia component should be dependent on both the morphological and magnetic properties.

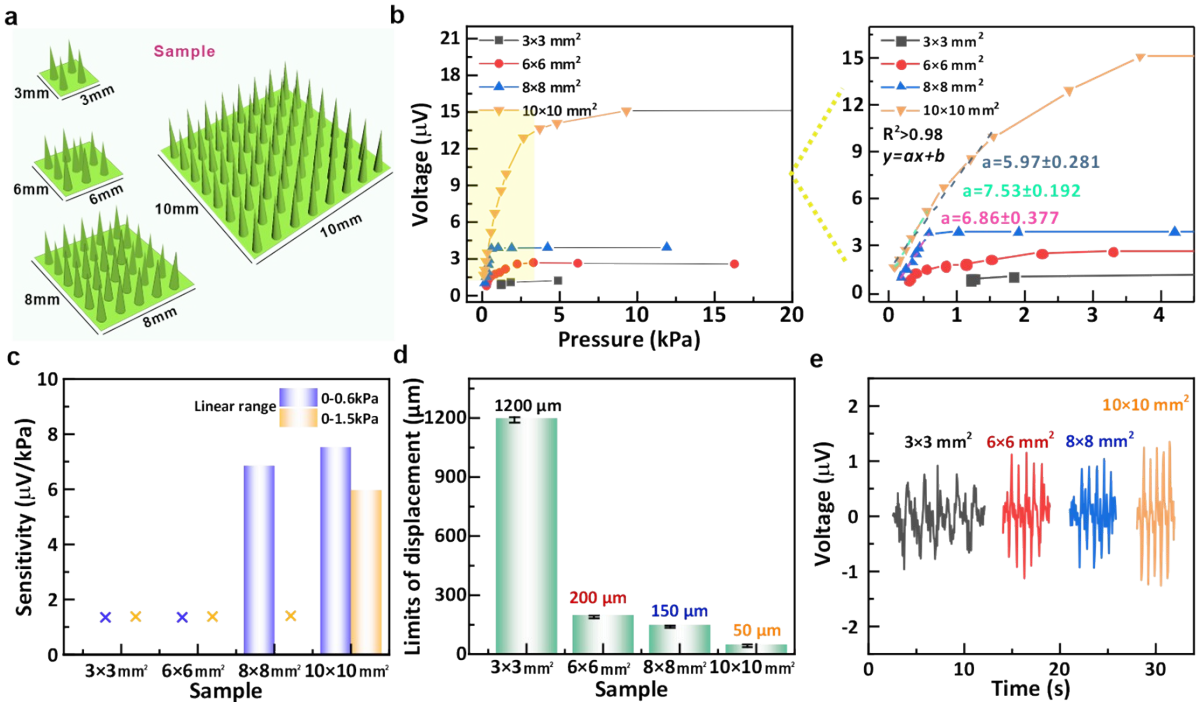

Figure S8. (a) Schematic diagram of MMCA samples with different micro-cilia areas of 3×3 mm^2, 6×6 mm^2, 8×8 mm^2 and 10×10 mm^2. (b) The real-time voltage signals within range of 0-20 kPa, with linear fitting in the lower pressure range. (c) Statistical results of the device sensitivity. (d) Detection limit of the MMCA devices, and (e) Real-time voltage signals corresponding to the detection limits from the devices with different areas.

To evaluate the effect of micro-cilia number on the sensing performance, we prepared four MMCA devices with different covering area. The areas of micro-cilia array were designed as 3×3 mm^2, 6×6 mm^2, 8×8 mm^2, and 10×10 mm^2. The linear fitting cannot be performed on the MMCA devices with smaller areas of 3×3 mm^2 and 6×6 mm^2 due to the weak signals that can be induced during the characterization process. The devices with area of 8×8 mm^2 and 10×10 mm^2 have good linearity in a smaller pressure range of 0-0.6 kPa (R^2>0.98), with the sensitivity of 6.86 kPa^{-1} and 7.53 kPa^{-1}. For a wider pressure range, only the MMCA device with area of 10×10 mm^2 exhibits linear sensing over 0-1.5 kPa with a sensitivity of 5.97 kPa^{-1}. The results indicate that the number of micro-cilia is positive to provide possible magnetic flux change during the bending process, which is critical to improve the signal amplitude for reliable sensing.

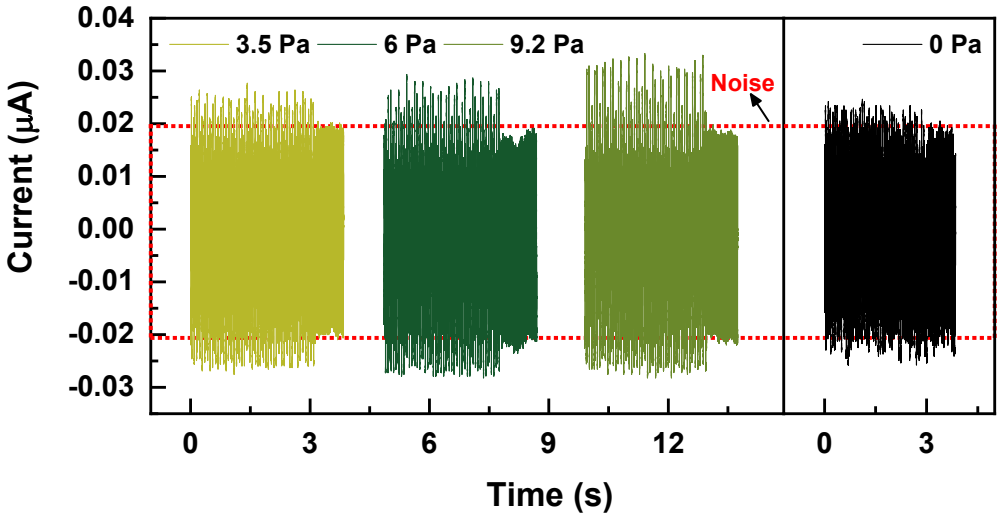

Figure S9. Real-time response of MMCA devices to ultra-low pressures 3.5 Pa, 6 Pa, and 9.2Pa. To ensure the authenticity and reliability of the data, the noise signals generated from the instrument were also provided alongside (0 Pa).

According to the principle of electromagnetic induction, the higher the mechanical stimulation frequency experienced by MMCA, the larger the voltage signals will be induced. Therefore, we used a vibrator to examine the detection limit of the device by increasing the vibration frequency of the loading. Here, a vibrational frequency of 30 Hz and a signal sampling rate of 100 Hz are set as the testing conditions. The figure shows the response of the micro-cilia to ultra-low pressure loads of 3.5 Pa, 6 Pa, and 9.2 Pa, and includes the signal when the vibrating instrument probe did not touch the micro-cilia (designated as 0 Pa) as a control group. Via excluding the noise from the signal acquisition equipment and the vibrator's own noise, the results indicate that the detection limit of the MMCA can be as low as 3.5 Pa.

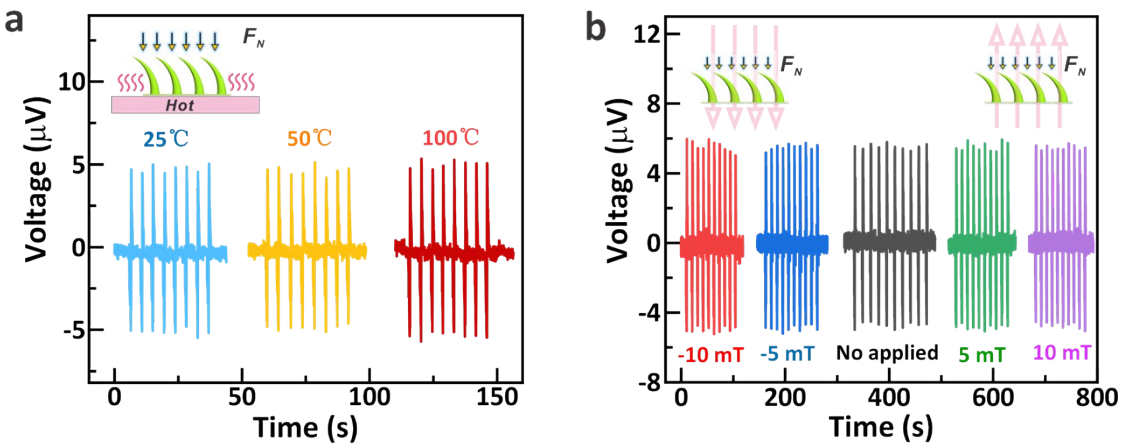

Figure S10. (a) Voltage intensities of the FBE-skin response to pressure at ambient temperatures of 25°C, 50°C, and 100°C. (b) The voltage signals with a weak magnetic field of ±5mT and ±10mT and no applied magnetic field.

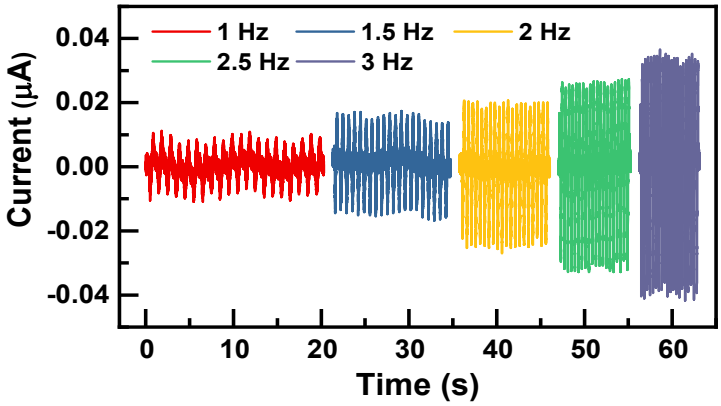

Figure S11. Real-time response of the MMCA device to periodic pressure of 1.35 kPa with 20 cycles and releasing under different frequencies (1 Hz, 1.5 Hz, 2 Hz, 2.5 Hz and 3 Hz).

As shown in the figure, the higher frequencies cause faster micro-cilia deformation and the changes in the magnetic flux, which in turn leads to larger output voltages based on the law of electromagnetic induction. The periodical signals also exhibit the consistent frequency with the input of the mechanical stimuli.

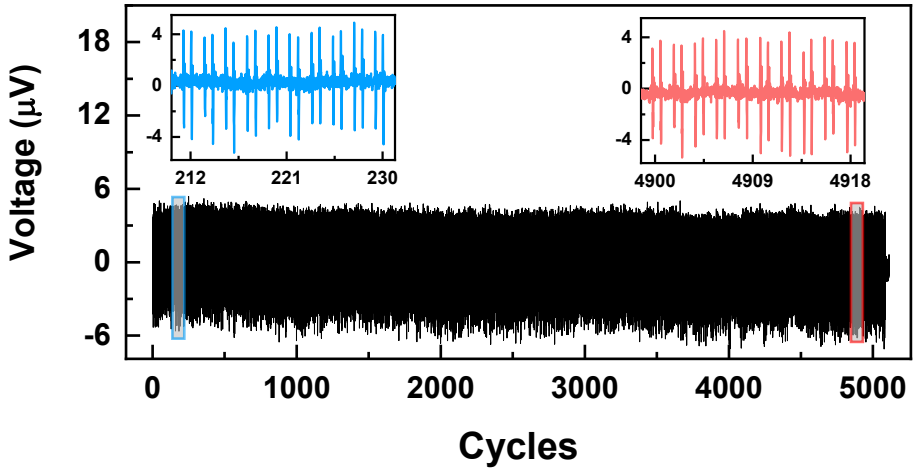

Figure S12. Long-term stability of the MMCA device when repeatedly sliding at a speed of 50 mm/s across the surface of a sliding platform for more than 5000 cycles.

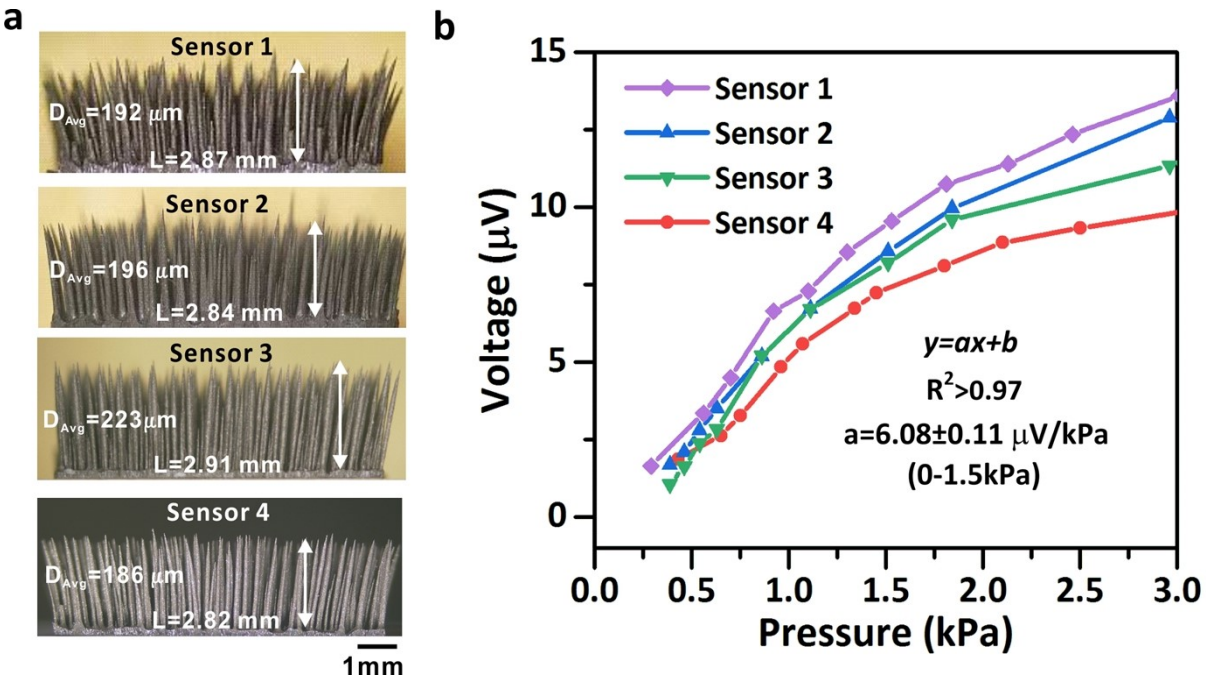

Figure S13. (a) Optical images of four MMCA devices under the same preparation conditions (m_{PDMS}: m_{CIP}: m_{NdFeB}=3:3:3), and (b) the output voltage response of four devices under different pressures.

We prepared four MMCA samples under the same experimental conditions. The micro-cilia distribution and morphology exhibit high repeatability (L/D=14.4±0.9). The sensitivity (6.08±0.11 $\mu V/kPa$) of the four self-assembled MMCA displays slight difference under the pressure range of 0-1.5 kPa. The results further convince the repeatable morphology of MMCA and the corresponding pressure sensing performance.

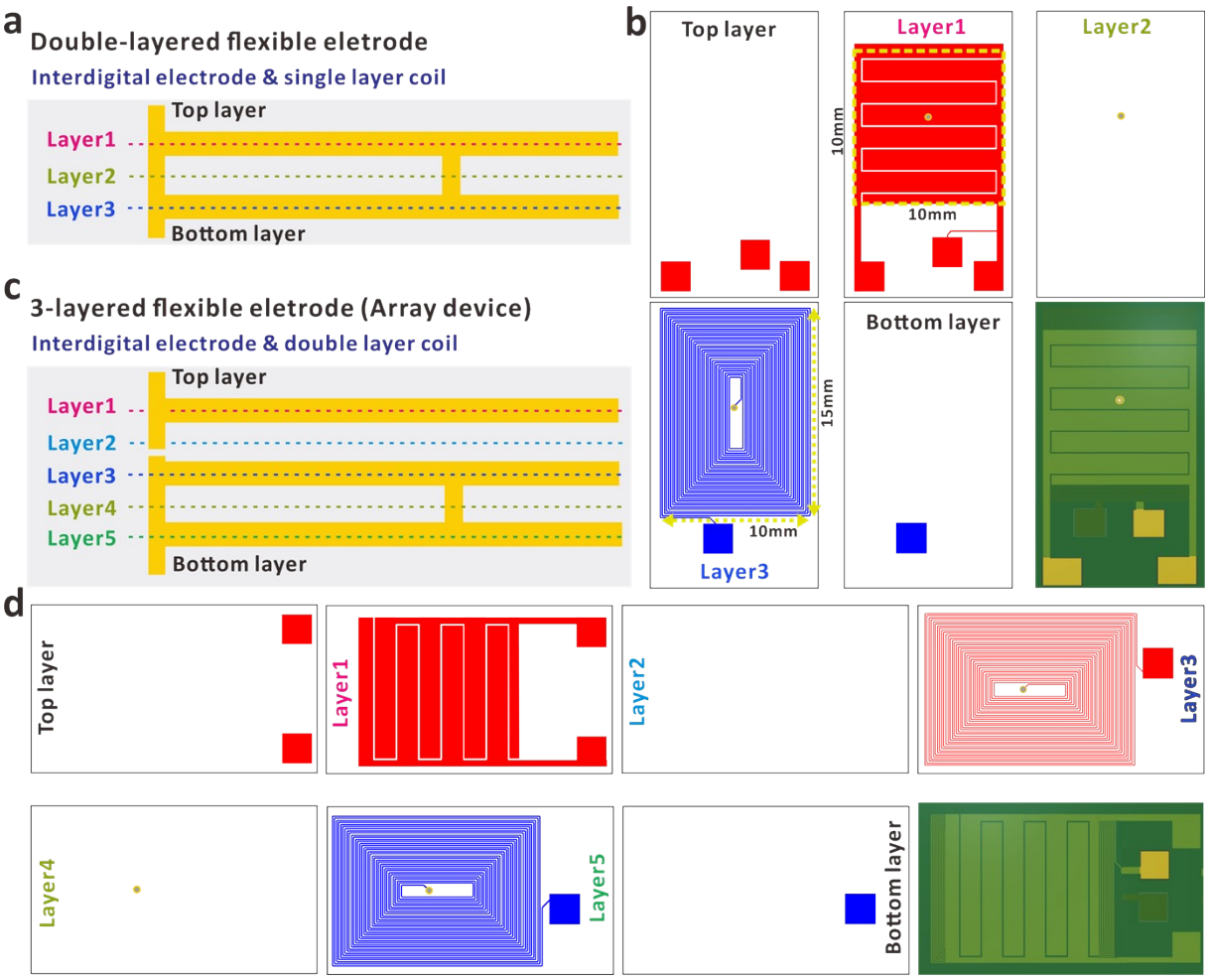

Figure S14. Schematic diagrams of the flexible electrodes. (a) Cross-sectional view of the double-layered flexible electrode. (b) The layout of connections between the corresponding conductive layers. The critical dimension of the electrodes is indicated in the diagram. (c) Cross-sectional view of the 3-layered flexible electrode. (d) The interconnection among the different conductive layers. The design of the flexible electrode unit for the arrays adopts the structure of the above three layers of electrodes.

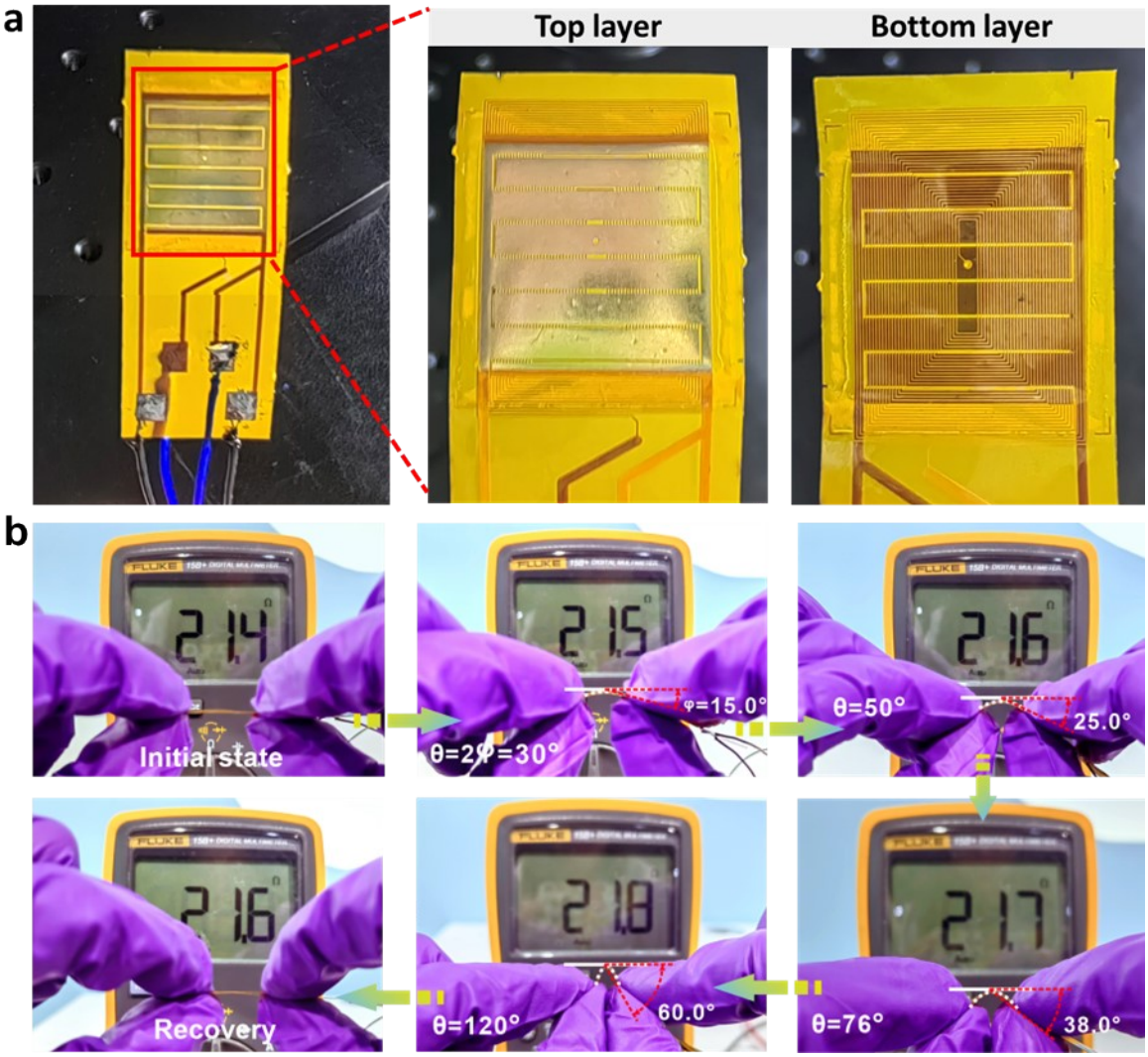

Figure S15. (a) The optical images of the double-layer flexible electrode. The top layer is interdigital electrodes for the MDA, and the bottom layer is coils for the MMCA. (b) Resistance stability of the double-layered coil electrode at different bending degrees of 30°, 50°, 76°, and 120°. The resistance values measured by the multimeter indicate the electrical stability of the coil when exposed to external mechanical deformations. Symbols of θ and φ have been indicated in the figures to explain the angles.

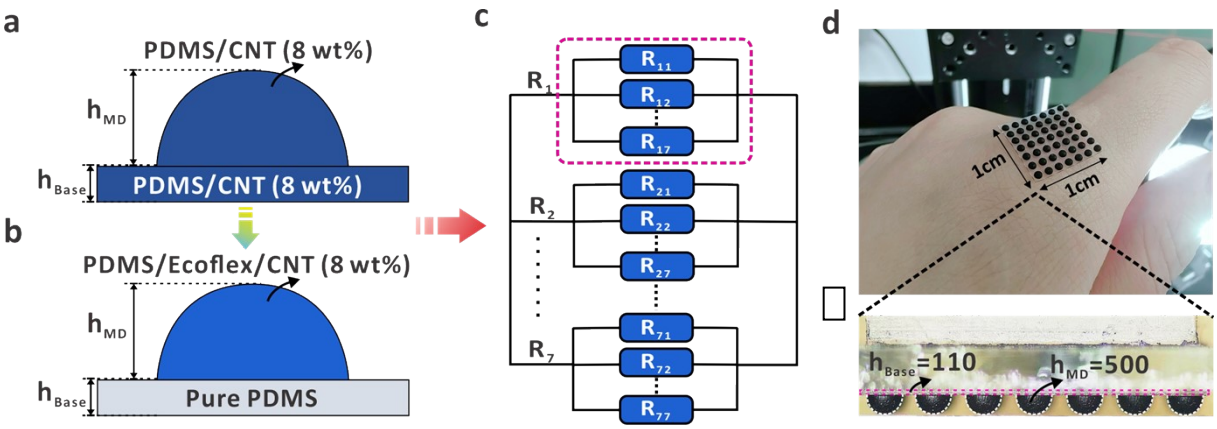

Figure S16. (a, b) Schematic diagrams showing the micro-dome components before and after the optimization. (c) Equivalent circuit of the micro-dome array device (rows and columns connected in parallel). (d) Optical image of the optimized MDA sensor with transparent pure PDMS layer as the substrate. (e) Magnified cross-sectional view of the MDA device, which consists of the conductive micro-domes and a transparent substrate.

This figure compares the geometry of the MDA with/without a conductive PDMS/CNT substrate (**Figure S16a, b**). Initially, we used the templating method to fill PDMS/CNT (8 wt%) mixed paste-like conductive slurry to simultaneously fabricate the structure and the base layer. The obtained base layer was pressed with a glass slide after slurry coating to ensure its flatness and we increased the coating volume appropriately during this process. From the preparation process described above, it is evident that the scraping technique poses certain difficulties and sacrifices the controllability of the base thickness to maintain its flatness. To address this issue, we further optimized the fabrication process of the MDA base layer to obtain a thinner and more conformable FBE-skin. Specifically, after preparing the micro-dome array, we directly spin-coated a pure PDMS gel onto the sample, resulting in a thin (110 μm), skin-friendly, and transparent base layer (**Figure S16d**). Additionally, the equivalent circuit diagrams of the MDA and the interdigital electrode assembly after the optimization are shown in **Figure S16c**. In the 7×7 MDA matrix, the rows and columns are connected in parallel (the equivalent resistance of the device is the parallel combination of all the resistances). Based on such configuration, the effect from the substrate can be avoided and the sensing behavior will be contributed by the design of the MDA.

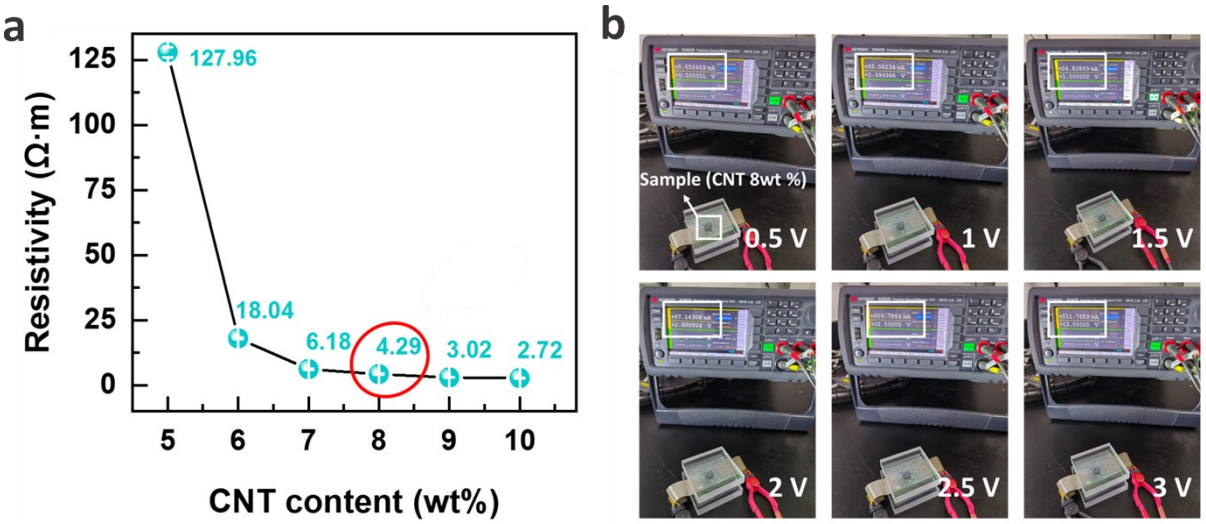

Figure S17. (a) Resistivity of the PDMS/CNT composites with different CNT contents. (b) Optical images of the resistivity test for the sample with CNT content of 8 wt%.

At the set voltage of 0.5 V, 1 V, 1.5 V, 2 V, 2.5 V and 3V, the corresponding currents were recorded respectively to obtain the I-V curve. Using the slope of this curve as the resistance, the final resistivity of the sample is obtained via introducing the dimension of the sample under measurement.

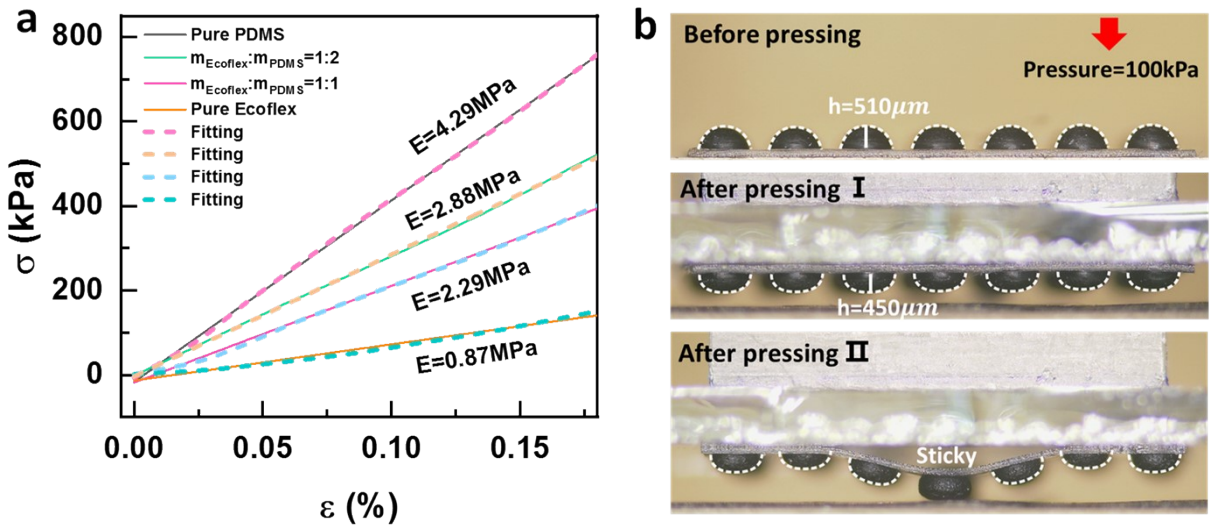

Figure S18. (a) Elastic moduli of PDMS/Ecoflex composite with different mass ratios. (b) Optical images of the micro-dome array prepared by pure Ecoflex under the loading and unloading of 100 kPa. After pressing, the micro-dome could not fully recover to the initial morphology (I) and exhibited a possibly sticking behavior due to the intrinsic viscous property (II).

For the pure Ecoflex™ 00-10, the Ecoflex™ instruction manual indicates that Ecoflex™ 00-10 can possibly cure with a "tacky" surface (http://www.smooth-on.com.cn/uploadfile/2018/0506/20180506092715429.pdf). Especially after unloading at a full-scale pressure (~100 kPa), we observed that the micro-dome structure of pure Ecoflex™ 00-10 obviously appeared the adhesion phenomenon II for a while. We considered that this was caused by the high normal pressure, even though the recovery might occur after a long time. As a result, we did not select pure Ecoflex™ 00-10 for the MDA fabrication.

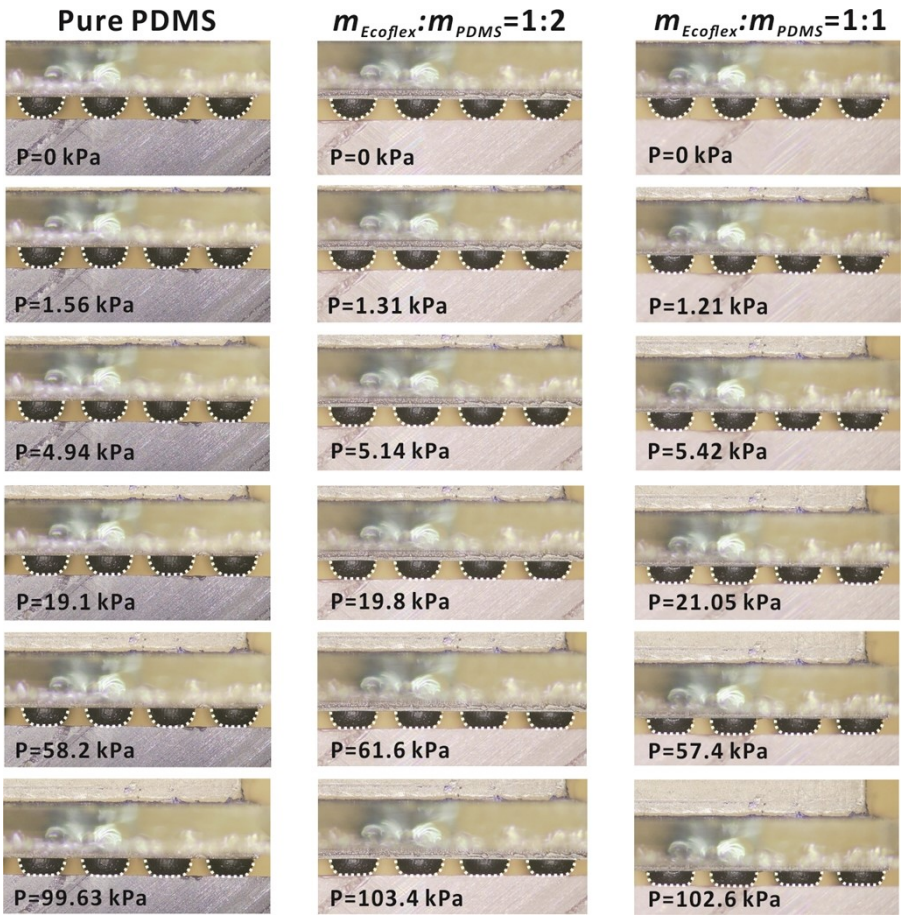

Figure S19. Typical optical images of the deformation process when the normal pressure was applied to the micro-domes prepared by pure PDMS, $m_{Ecoflex}$: m_{PDMS}=1:2, and $m_{Ecoflex}$: m_{PDMS}=1:1.

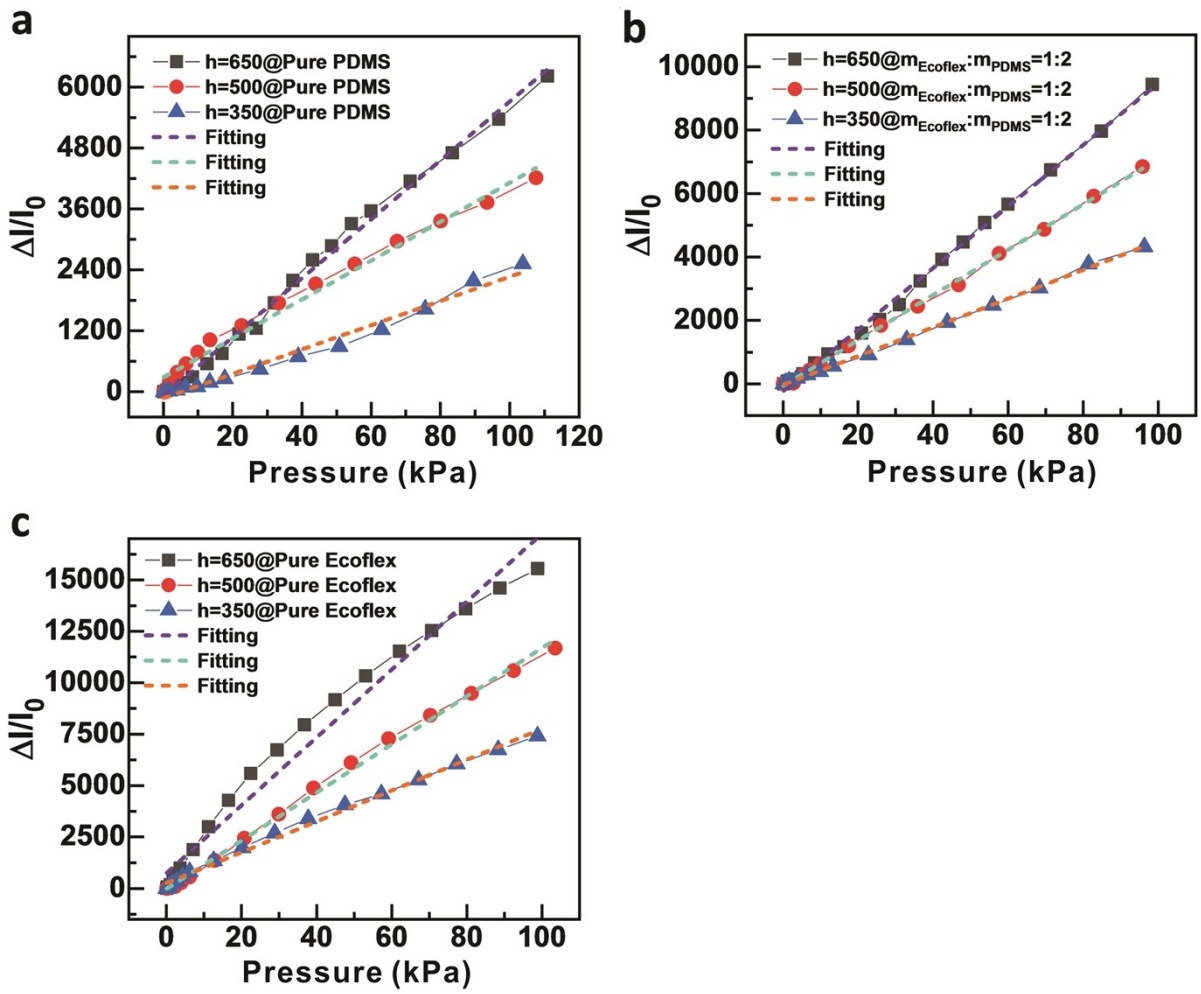

Figure S20. Corresponding current variations of the MDA devices under different pressures. The MDA devices with heights of 350 μm, 500 μm and 650 μm was prepared by PDMS and Ecoflex with different mass ratios of (a) Pure PDMS, (b) $m_{Ecoflex}$: m_{PDMS}=1:2, and (c) Pure Ecoflex.

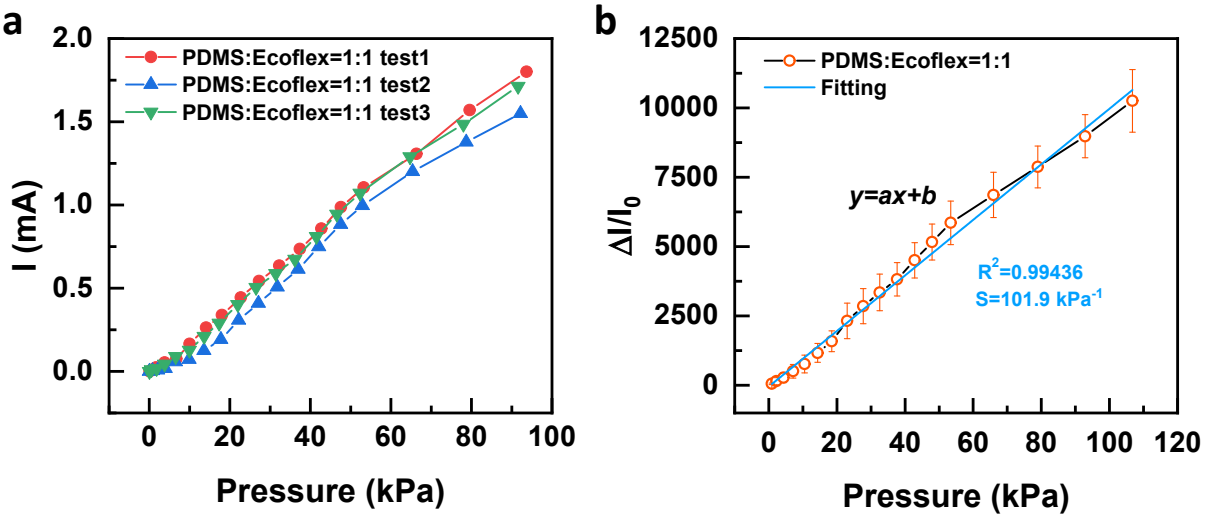

Figure S21. (a) The electrical current and (b) Relative current variation of the same micro-dome device in multiple tests.

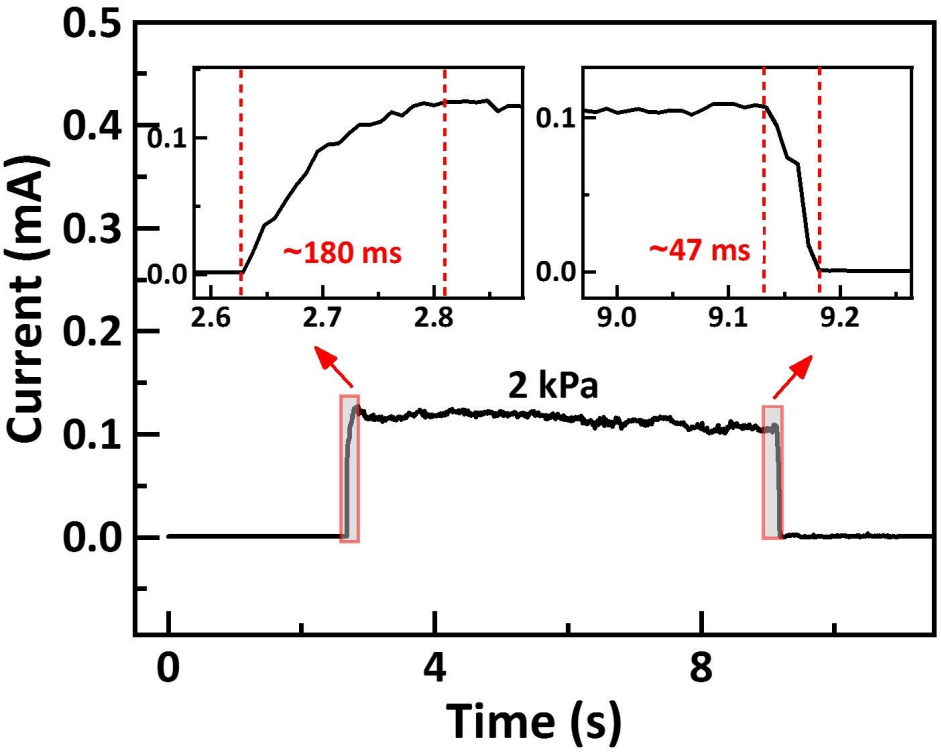

Figure S22. The response time and recovery time of MDA under pressure loading speed of 30 mm/s.

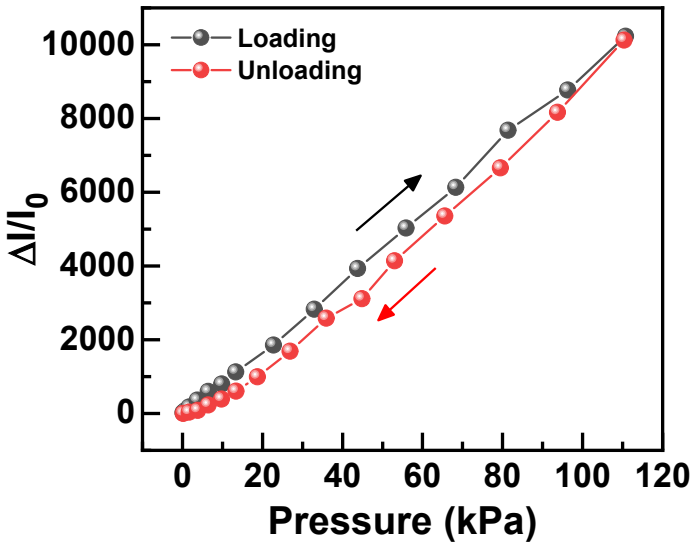

Figure S23. Relative change in the current of a micro-dome-shaped device in the loading-unloading pressure to show the behavior of hysteresis.

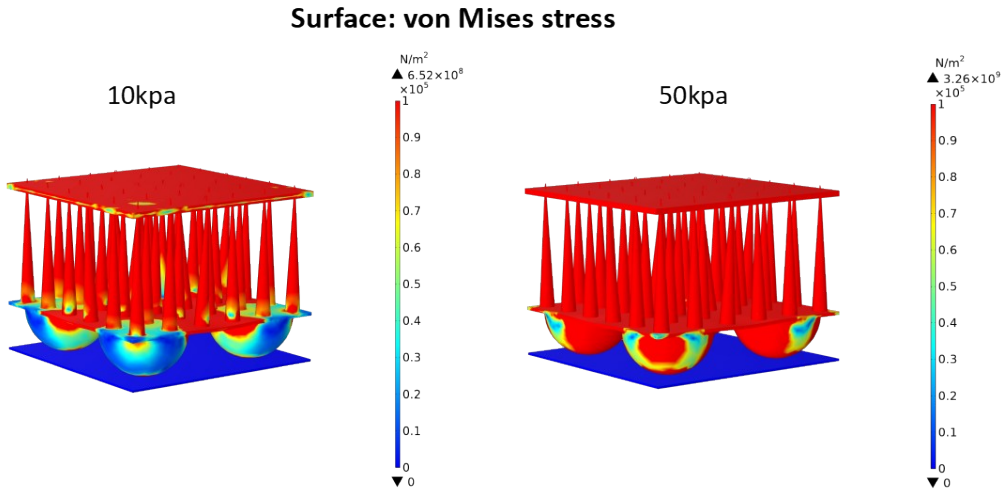

Figure S24. Simulated mechanical distribution of the FBE-skin under normal pressures of 10 kPa and 50 kPa.

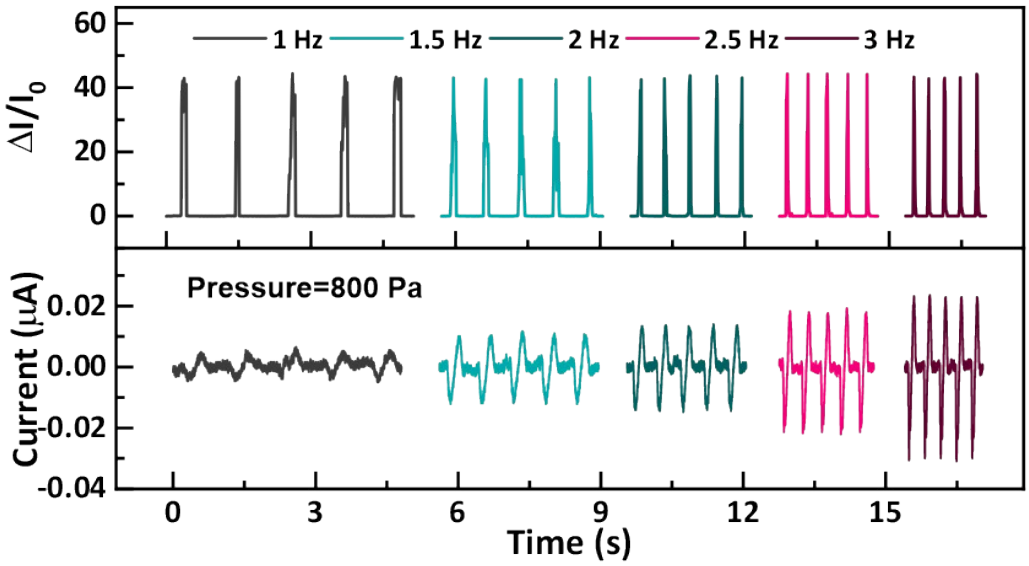

Figure S25. The real-time signal of the FBE-skin with a pressure of 800 Pa under different frequencies of 1 Hz, 1.5 Hz, 2 Hz, 2.5 Hz, and 3 Hz.

The dual-channel signals are in a high degree of synchronization, indicating the simultaneous deformation during the application of the mechanical stimuli. Also, the current variation is identical under such low frequencies because the magnitude is mainly caused by the force magnitude.

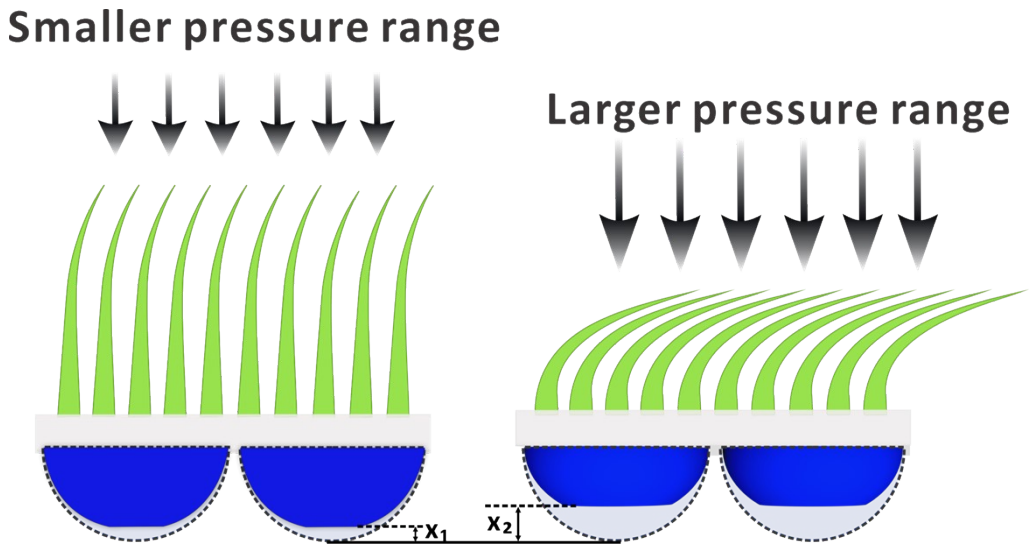

Figure S26. Schematic diagram of the compressive deformation of micro-dome structure before and after saturation of the micro-cilia deformation under low and high pressures.

From top to bottom, the FBE-skin consists of the MMCA structure for sensing of high-frequency dynamic information, and the MDA for static mechanical stimuli within a single unit. We recorded the voltage and current signals output by the FBE-skin under different pressures (**Figure 4e**). The current signals revealed that the overall sensitivity at pressures of 3.22 kPa and 5.02 kPa was affected by the MMCA on top, where this lower pressure range mainly falls before the saturated deformation of the MMCA. The deformed micro-cilia array served as a buffer layer to reduce the pressure that was directly applied on the MDA layer, resulting in smaller compressive deformation X_1 (small current change) under lower pressures. However, when the pressure is further increased to 7.2 kPa, the buffering effect of the micro-cilia becomes less significant because of saturation of the MMCA layer. The micro-dome structures thus experienced larger compressive deformation $X_2 > X_1$, causing a significant current variation that is corresponding to the intrinsic sensing capability. Overall, even though the coupling of MMCA might affect the sensitivity of the MDA component under low-pressure range, the introduced MMCA layer serves to achieve in-plane tangential force perception and compensates the responsive limitation at high-frequency range.

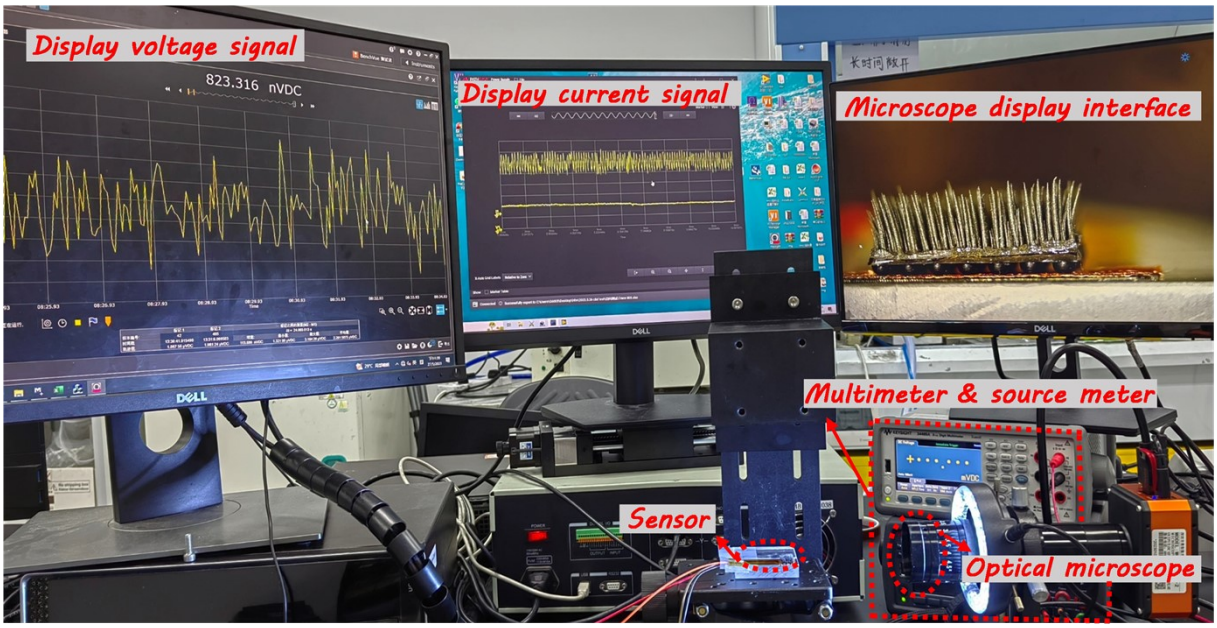

Figure S27. The overall platform for the standard characterization to evaluate the performance of the FBE-skin.

The digital multimeter was used to record real-time voltage signals and the high-precision source meter is employed to obtain current signals. The side-view optical image was captured by a customized optical microscopy, which records the deformation of the micro-structures in real-time. The sensor was put on the stage and the mechanical stimuli were applied to deform the device for signal generation. We notice that currently we need to rely on commercial large-scale equipment to complete the data acquisition process due to the relatively low output signals. To advance the practical application of this technology and ensure its effectiveness in real-world scenarios, we can explore the following potential solutions: (1) Development of Low-Cost Integrated Circuits: via design of low-cost integrated circuits (IC) to capture signals from the E-skin, and to utilize high-sensitivity amplifiers and analog-to-digital converters (ADC) to capture and amplify the output signals. These components are relatively inexpensive and easy to integrate, ensuring measurement accuracy and reliability. (2) Wireless Transmission Technology: by employing wireless transmission technologies, such as Bluetooth or Zigbee, to send signals to portable devices for signal processing to relieve the burden on costly acquisition systems.

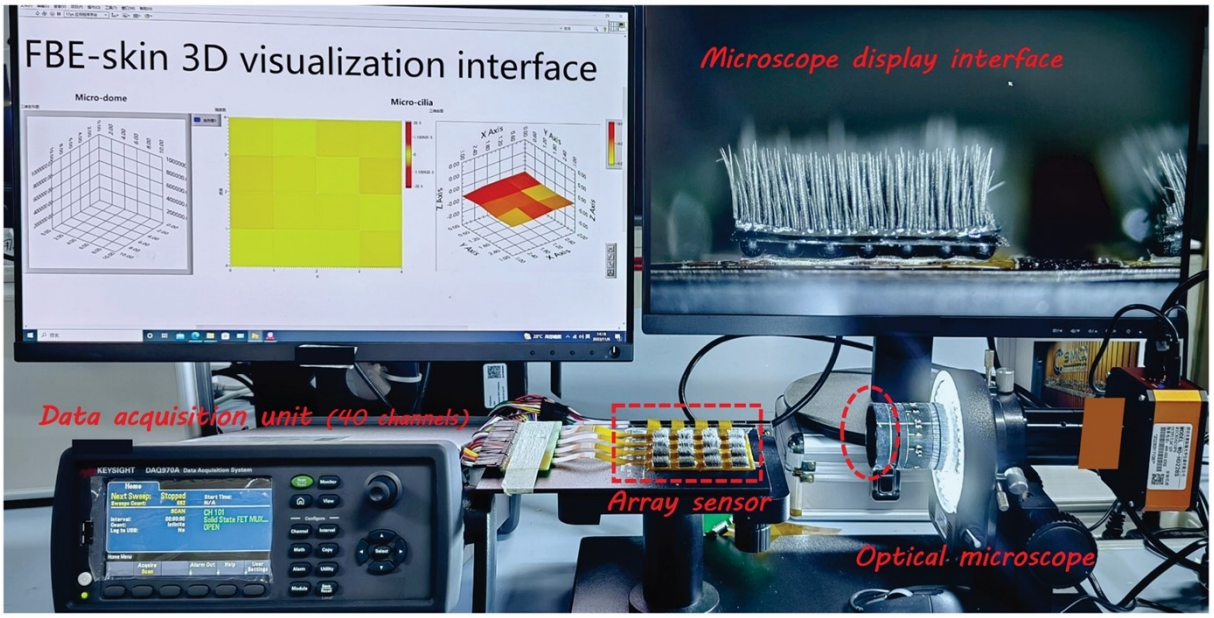

Figure S28. The experimental platform of 3D visualization and decoding system based on the FBE-skin array.

A 4×4 FBE-skin array was designed for the demonstration of stimuli perception. The signals from the MMCA and MDA branches can be obtained simultaneously and transmitted to the software interface to finalize the visualization process. At the same time, a customized optical microscope system was applied to observe the deformation of the FBE-skin in real-time. The optical image in the top-right corner shows a cross-sectional view of the FBE-skin, which is composed of the micro-cilia on top and the micro-domes at the bottom.

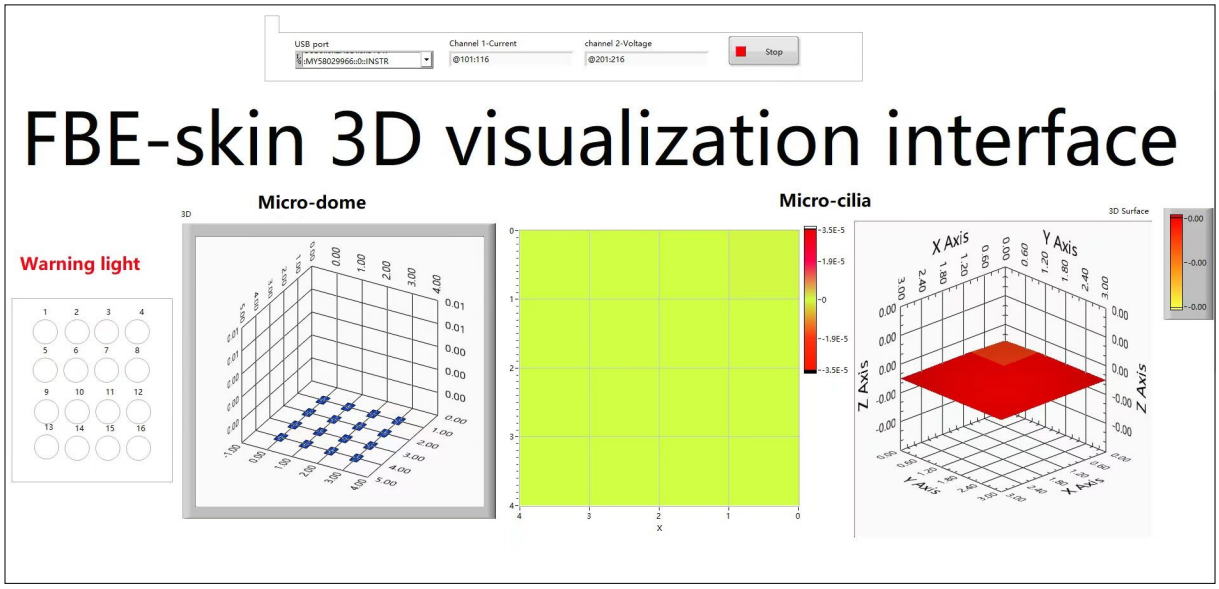

Figure S29. The customized 3D visualization interface for FBE-skin array.

The interface includes the signal visualization from the micro-dome (MDA) and the micro-cilia (MMCA). Apart from the position determination, the signal intensity can also be reflected from the color or the height of the histograms. Furthermore, the warning lights are designed to mimic the warning function. Each pixel of the warning light is related with a specific FBE-skin. When the deformation of MDA causes the electrical signal that exceeds the threshold, a warning will be released, and the corresponding light will be on as green (moderate pressure) and red (large pressure).

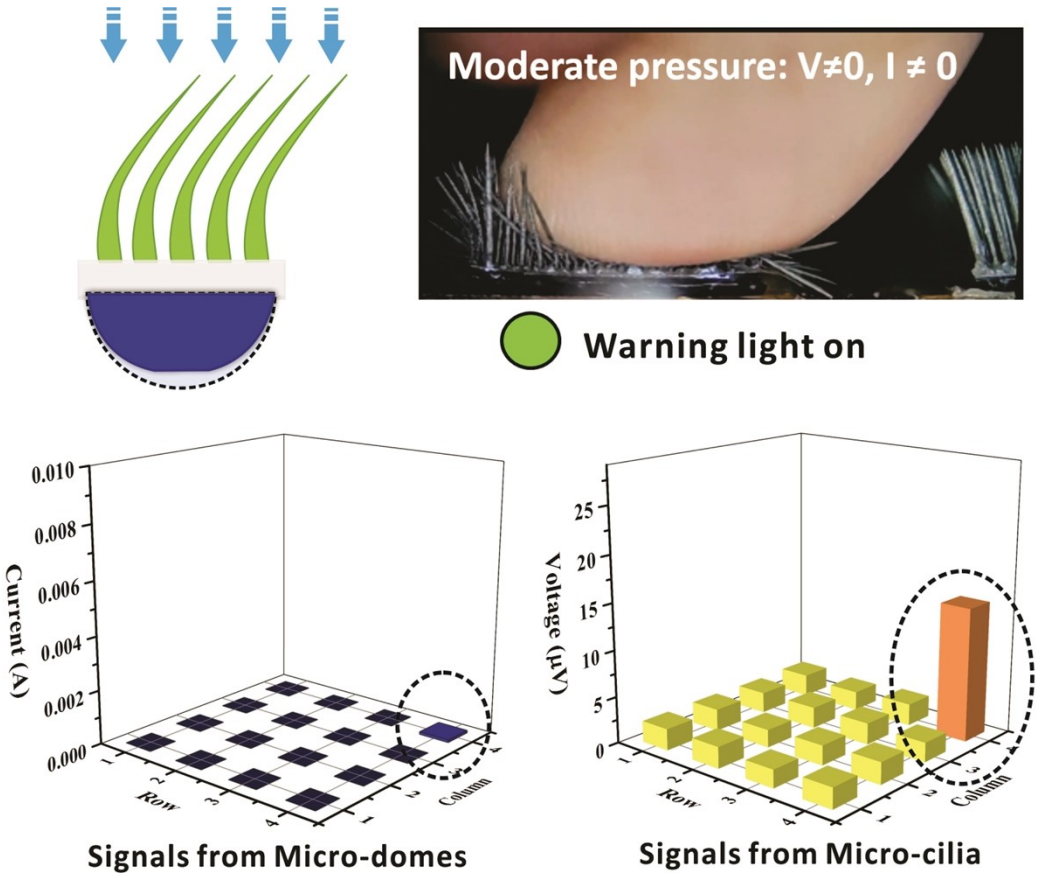

Figure S30. Schematic diagram of the FBE-skin deformation when a moderate pressure was applied. Related electrical signals from the micro-domes and micro-cilia were provided.

Based on this applied pressure, both the micro-cilia and micro-dome were deformed as shown in the optical image. Consequently, the currents from the micro-domes are non-zero, and the induced voltage from the micro-cilia provides the information of the MMCA bending. As the current signal is relatively weak, a green light will be on, indicating the potential harm to the FBE-skin.

Supplementary Notes.

Supplementary Note S1: Theoretical analysis of the piezoresistive component.

The relationship between the sensing sensitivity and dimensional parameters of micro-dome-based pressure sensing unit is analyzed herein. For the presented sensor configuration (**Figure S31**), the total resistance of the sensor consists of the bulk resistance from the micro-dome structure (R_b), and the contact resistance between the coplanar electrodes and the micro-dome structures (R_c). As the contact resistance is much larger than the bulk resistance, the total electric resistance (R) can be simplified as[1, 2]

$$R = 2R_c + R_b \approx R_C.$$

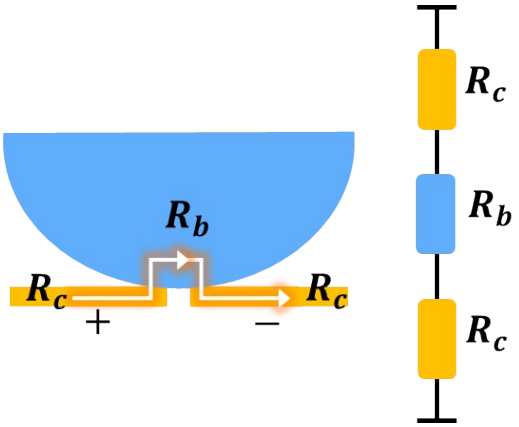

Figure S31. Equivalent diagram of the total contact resistance between the micro-dome and the interdigital electrode.

From this perspective, the variation of the electric resistance is mainly determined by the effective contact area between the micro-domes and the coplanar electrodes. For the dome-shaped square arrays, a parallel circuit is formed between the micro-domes and the interdigital electrode. We thus have

$$\frac{1}{R} = \frac{1}{R_{C1}} + \frac{1}{R_{C2}} + \ldots + \frac{1}{R_{Cn}} = \sum_{i=1}^{N} \frac{1}{R_{Ci}} = \frac{N}{R_C},$$

where R_{Ci} is the contact resistance of individual dome with the coplanar interdigitated electrode and N is the total effective number of the micro-domes. According to the Holm theory[3, 4] of the contact resistance, we have

$$R_{Ci} = \frac{\rho}{Nd}$$

where ρ is the electrical resistivity of as-prepared micro-dome, d is the diameter of circular contact interface of domes within the area that is under consideration. With the constant voltage V, the initial electric current of

$$I_0 = \frac{V}{R_0}$$

and under a typical pressure, the electric current changes to $I = \frac{V}{R}$. We then have

$$\frac{\Delta I}{I_0} = \frac{d_1 - d_0}{d_0} = \frac{d_1}{d_0} - 1$$

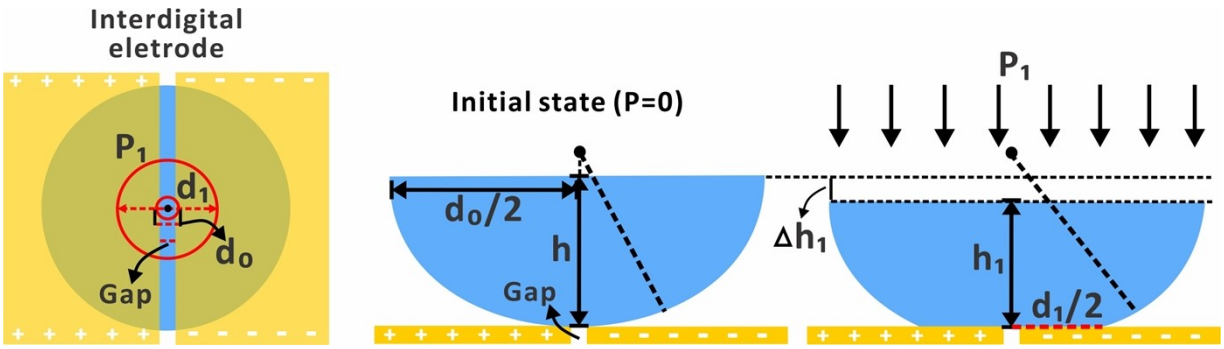

Figure S32. Structural deformation of the micro-dome under different pressure loadings.

Figure S32 shows the dome-shaped structure with height of h and bottom diameter d_0. With external pressure (P_1) in the normal direction, the semi-sphere will undergo small compressive deformation (Δh_1), resulting in the circular contact area increase between the micro-dome and the electrodes with diameter of d_1. And here, the pressed semi-sphere is regarded as a cylinder with equivalent diameter and cross-sectional area. According to Hooke's law and the definition

of elastic modulus, we have $\Delta P = E\left(\frac{\Delta h}{h}\right)$, where ΔP is the external pressure, E is the elastic modulus, and $\frac{\Delta h}{h}$ is the relative compression. Thus, the sensitivity of the pressure sensor can be explained as,

$$S = \frac{\delta\left(\frac{\Delta I}{I_0}\right)}{\delta(\Delta P)} = \left(\frac{I_1 - I_0}{I_0}\right).\frac{h}{E\Delta h} = \left(\frac{d_1}{d_0} - 1\right).\frac{h}{E\Delta h_1}$$

For the dome structures in this study, the interdigital gap of the interdigital electrode is fixed at 100 μm. We assume that the interdigital electrode and the micro-dome form a closed-loop circuit in the initial state, and the effective contact area between them is a small circle with radius d_0 which can be approximated as a constant. On one hand, the contact resistance is adjusted synchronously with the radius of the contact surface. On the other hand, a higher sensitivity can be obtained if with a higher height of the micro-dome or the smaller elastic modulus based on the above formula. In addition, it can be found that the sensitivity closely depends on the contact radius of the initial state, and a smaller initial contact radius may yield higher sensitivity because of the larger initial resistance. This conclusion may provide a theoretical support to design the flexible sensor with higher sensitivity based on the conductive micro-dome structures.

Supplementary Note S2: COMSOL simulation for mechanical property of FBE-skin.

A simplified 3D structural model was established using COMSOL Multiphysics software (**Figure S24**). The model consists of an array of micro-cilia (with an aspect ratio of 14) in a 6×6 configuration, and a spacing of 3500 μm between the adjacent micro-cilia. Additionally, an array of micro-domes was arranged in a 4×4 pattern, with a distance of 1000 μm between two neighboring micro-domes. For simulation convenience, the materials used for the MMCA and the MDA are both PDMS (Elastic modulus is 750 kPa, Poisson's ratio is 0.49). The rectangular regions above the micro-cilia array and below the MDA are defined as silica materials and are respectively set as the boundary load-controlled surface and the fixed constraint surface. The mesh environment was established using refined tetrahedral elements. The solid mechanics module of structural mechanics is employed to track the stress. The governing equations are defined as $S \cdot n = F_A$ and $F_A = \frac{F_{tot}}{A}$, where F_{tot} represents the total force applied, F_A is the total force per unit area, S represents the force vector per unit area, A represents the size and n is the normal vector of the surface element. By computing these quantities, the force distribution of the FBE-skin under different normal pressures can be obtained.

Supplementary Tables.

Table S1. Statistics on the aspect ratio, device sensitivity, and detection limit of micro-cilia arrays prepared by PDMS, CIP, and NdFeB with different mass ratios. Here, L is the length of the micro-cilia, D is the bottom diameter of the micro-cilia, and L/D is defined as the aspect ratio.

m_{PDMS}: m_{CIP}: m_{NdFeB}	Ratio of NdFeB (wt %)	L (mm), D (μm), and L/D (average)	Sensitivity ($\mu V/kPa$)	Detection limit (Pa)
3:2:2	28.6	L=1.82±0.16 D=201±20 L/D=9.1	5.34 (0-1.8kPa)	300
3:2:3	37.5	L=1.48±0.20 D=227±35 L/D=6.5	0.29 (0-12 kPa)	420
3:2:4	44.4	L=1.59±0.45 D=218±65 L/D=7.3	0.52 (0-4.5 kPa)	500
3:2:5	50	L=1.62±0.69 D=278±95 L/D=5.8	1.04 (0-10 kPa)	60
3:3:3	33.3	L=2.87±0.15 D=192±25 L/D=15.0	6.12 (0-1.5 kPa)	210
3:5:5	38.5	L=3.11±0.18 D=142±25 L/D=21.8	5.59 (0-1 kPa)	140

Table S2. Summarized sensitivity and sensing linearity of the MDA device with varying heights of the micro-domes.

Mass ratios	Heights of micro-dome (μm)	Sensitivity (kPa^{-1}): 0-100 kPa	Linearity (R^2)
Pure PDMS	h=650	58.0±9.0	0.99
	h=500	36.3±2.0	0.99
	h=350	23.9±5.0	0.99
$m_{Ecoflex}$: m_{PDMS}=1:2	h=650	97.1±2.0	0.98
	h=500	66.8±5.0	0.98
	h=350	45.3±1.5	0.99
$m_{Ecoflex}$: m_{PDMS}=1:1	h=650	140.5±4.0	0.98
	h=500	96.6±5.0	0.99
	h=350	61.5±2.0	0.99
Pure Ecoflex	h=650	165.0±8.0	0.97
	h=500	126.2±9.0	0.98
	h=350	74.9±2.0	0.99

Supplementary References.

1. D. Geng, S. Chen, R. Chen, Y. You, C. Xiao, C. Bai, T. Luo and W. Zhou, *Adv. Mater. Technol*., 2021, **7**, 2101031.
2. H. Li, K. Wu, Z. Xu, Z. Wang, Y. Meng and L. Li, *ACS Appl. Mater. Interfaces*, 2018, **10** 20826-20834.
3. R. Holm, Electric Contact: Theory and Application, 4th ed., Springer-Verlag, New York, **1976**, pp.10-12.
4. B. N. J. Persson, *Tribol. Lett.*, 2022, **70**, 88.